INTERNATIONAL JOURNAL FOR NUMERICAL METHODS IN ENGINEERING
Int. J. Numer. Meth. Engng. 2000; **48**:211–237

Boundary element analysis of three-dimensional cracks in anisotropic solids

Ernian Pan[1] and F. G. Yuan[2,*,†]

[1] *Structures Technology, Inc., Cary, NC 27511, U.S.A.*
[2] *Department of Mechanical and Aerospace Engineering, North Carolina State University, Raleigh, NC 27695, U.S.A.*

SUMMARY

This paper presents a boundary element analysis of linear elastic fracture mechanics in three-dimensional cracks of anisotropic solids. The method is a single-domain based, thus it can model the solids with multiple interacting cracks or damage. In addition, the method can apply the fracture analysis in both bounded and unbounded anisotropic media and the stress intensity factors (SIFs) can be deduced directly from the boundary element solutions.

The present boundary element formulation is based on a pair of boundary integral equations, namely, the displacement and traction boundary integral equations. While the former is collocated exclusively on the uncracked boundary, the latter is discretized only on one side of the crack surface. The displacement and/or traction are used as unknown variables on the uncracked boundary and the relative crack opening displacement (COD) (i.e. displacement discontinuity, or dislocation) is treated as a unknown quantity on the crack surface. This formulation possesses the advantages of both the traditional displacement boundary element method (BEM) and the displacement discontinuity (or dislocation) method, and thus eliminates the deficiency associated with the BEMs in modelling fracture behaviour of the solids. Special crack-front elements are introduced to capture the crack-tip behaviour. Numerical examples of stress intensity factors (SIFs) calculation are given for transversely isotropic orthotropic and anisotropic solids. For a penny-shaped or a square-shaped crack located in the plane of isotropy, the SIFs obtained with the present formulation are in very good agreement with existing closed-form solutions and numerical results. For the crack not aligned with the plane of isotropy or in an anisotropic solid under remote pure tension, mixed mode fracture behavior occurs due to the material anisotropy and SIFs strongly depend on material anisotropy. Copyright © 2000 John Wiley & Sons, Ltd.

KEY WORDS: boundary element method; fracture mechanics; stress intensity factor; crack opening displacement; dislocations

* Correspondence to: F. G. Yuan, Department of Mechanical and Aerospace Engineering, North Carolina State University, Raleigh, NC 27695, U.S.A.
† E-mail: yuan@eos.ncsu.edu

Contract/grant sponsor: National Science Foundation; contract/grant number: CMS-9713559
Contract/grant sponsor: Air Force Office of Scientific Research; contract/grant numbers: F33615-97-C-5089, F49620-98-1-0104

Received 15 September 1998
Revised 21 January 1999

INTRODUCTION

The boundary element method (BEM) is particularly attractive for linear elastic fracture mechanics [1, 2] in which SIFs and other fracture parameters play an important role in characterizing fracture behaviour of the solids. Accurate evaluation of singular state of stress near a crack tip has challenged all the numerical modelling techniques. Especially for the conventional BEM, the geometric coincidence of opposite nodes across the crack surfaces provides identical equations for these nodal points. This yields a rank deficient coefficient matrix. To circumvent this difficulty, several methods within the scope of BEM have been suggested [3]. These include the special Green's function method [4] where the crack surface conditions are embedded into the Green's function; the multi-domain technique [5] where each crack surface belongs to a distinct subregion; the displacement discontinuity or dislocation method [6, 7]; and the Galerkin symmetric method [8].

Recently, several single-domain BEMs have been proposed for the study of cracked media [3]. These single-domain BEMs involve two sets of boundary integral equations (one is the displacement integral equation, and the other is the traction type integral equation). One form of the single-domain BEMs is the so-called Dual Boundary Element Method (DBEM) where the displacement integral equation is collocated on the finite uncracked boundary and on one side of the crack surface, while the traction integral equation is collocated on the other side of the crack surface. This DBEM has been developed for both two-dimensional [9] and three-dimensional [10] isotropic cracked media, and it has been applied to various fracture mechanics problems [2].

In the DBEM formulation, the displacements on each side of the crack surface are collocated as unknown variables, which may be unnecessary for the SIF calculation. Therefore, an ideal single-domain BEM formulation would be the one, which requires discretization only on one side of the crack surface. Applying the displacement integral equation to the uncracked boundary only, and the traction integral equation on one side of the crack surface can achieve such single-domain BEM formulation. This single-domain BEM formulation has been proposed by Pan and Amadei [11] and Pan [3] for two-dimensional anisotropic cracked solids. A similar formulation was proposed recently by Qin *et al.* [12] for three-dimensional isotropic cracked solids in which the finite-part integral involved was evaluated exactly. The advantages of using this new single-domain BEM formulation are two-fold: (i) the Cauchy-type singularity in the displacement integral equation can still be calculated directly by the rigid-body motion method; and (ii) for cracks in an infinite domain, only the traction integral equation is needed to model the problem [3]. The traction integral equation for infinite domain problems resembles the displacement discontinuity or dislocation method, as has been investigated for some three-dimensional fracture problems [13–20].

Although BEM has been widely applied to various fracture problems in three-dimensional isotropic solids, relatively little attention has been paid to the three-dimensional anisotropic case [21] as to the authors' knowledge. A penny-shaped or elliptical crack in a linear elastic solid in an infinite three-dimensional space under a far-field stress or uniform traction along the crack surfaces, exact stress intensity factors for modes I, II, and III are available for either an isotropic solid or a transversely isotropic solid with the plane of isotropy coincident with the plane of the crack surface [22–24]. However, when the plane of isotropy is not aligned with the crack surface, the SIFs for an elliptical crack in an infinite anisotropic solid can only be expressed by an integral [23]. If the material property, geometry and boundary conditions are symmetric with respect to

the crack surface, the displacement integral equation can be employed to analyse some of the restricted 3-D crack problems in anisotropic media [25].

In this paper, we present a single-domain BEM formulation for linear elastic fracture mechanics analysis in three-dimensional anisotropic solids. This formulation is an extension of two-dimensional analysis [3] to the three-dimensional case and it is similar to Qin *et al.* [12] but extended to anisotropic solids. In this formulation, the displacement integral equation is collocated on the uncracked boundary and the traction integral equation on one side of the crack surface. The Cauchy-type singularity involved in the displacement integral equation is calculated directly by the rigid-body motion method; the finite-part integral associated with the traction boundary integral equation is evaluated by Kutt's numerical quadrature [26, 27]. To illustrate the utility of the method, numerical examples are carried out for a penny-shaped and a square-shaped crack in transversely isotropic, orthotropic and anisotropic solids. The SIF values are in good agreement with previously published results. Strong dependency of the SIFs on the material anisotropy is demonstrated in the numerical examples.

BEM FORMULATION FOR THREE-DIMENSIONAL ANISOTROPIC CRACKED SOLIDS

For a linearly elastic medium, we express the total displacements, stresses, and tractions through linear superposition as follows:

$$u_i^t = u_i^h + u_i^p, \quad \sigma_{ij}^t = \sigma_{ij}^h + \sigma_{ij}^p, \quad T_i^t = T_i^h + T_i^p \tag{1}$$

where the superscript t denotes the total solution, h the homogeneous solution, and p a particular solution corresponding to the body forces and/or the far-field stresses. The advantage of using the linear superposition (1) is the exact handling for the infinite domain problem, as will soon become clear.

Following the procedure of Pan and Amadei [28] one can show that the total internal displacement solution at $\mathbf{x}_p$ can be expressed by the following integral

$$\begin{aligned} u_i^t(\mathbf{x}_p) = & -\int_S T_{ij}^*(\mathbf{x}_p, \mathbf{x}_S) u_j^t(\mathbf{x}_S)\, \mathrm{d}S(\mathbf{x}_S) + \int_\Gamma T_{ij}^*(\mathbf{x}_p, \mathbf{x}_{\Gamma^+}) [u_j^t(\mathbf{x}_{\Gamma^+}) - u_j^t(\mathbf{x}_{\Gamma^-})]\, \mathrm{d}\Gamma(\mathbf{x}_{\Gamma^+}) \\ & + \int_S U_{ij}^*(\mathbf{x}_p, \mathbf{x}_S) T_j^t(\mathbf{x}_S)\, \mathrm{d}S(\mathbf{x}_S) + \int_S T_{ij}^*(\mathbf{x}_p, \mathbf{x}_S) [u_j^p(\mathbf{x}_S) - u_i^p(\mathbf{x}_p)]\, \mathrm{d}S(\mathbf{x}_S) \\ & - \int_S U_{ij}^*(\mathbf{x}_p, \mathbf{x}_S) T_j^p(\mathbf{x}_S)\, \mathrm{d}S(\mathbf{x}_S) \end{aligned} \tag{2}$$

where U_{ij}^* and T_{ij}^* represent the Green's functions for displacements and tractions which are given exactly for a transversely isotropic solid with arbitrarily oriented isotropic plane (see Appendix A), and are given explicitly for a generally anisotropic solid (see Appendix B); summation from 1 to 3 is implied on the repeated index; S and Γ ($\Sigma\Gamma_i$) are the uncracked boundary of the body and the crack surfaces, respectively, with the corresponding points being distinguished by subscript S and Γ (Figure 1); and a point on the positive (or negative) side of the crack is denoted by $\mathbf{x}_{\Gamma^+}$ (or

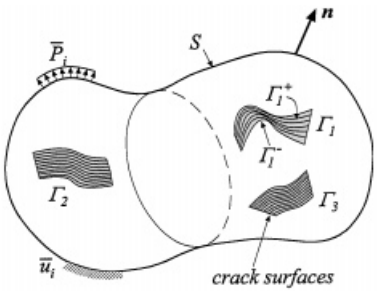

Figure 1. Geometry of three-dimensional cracks in an anisotropic body. S is the uncracked boundary; Γ_i^+ and Γ_i^- are the two sides of the crack surfaces Γ_i.

$\mathbf{x}_{\Gamma^-}$); In deriving Equation (2), we have assumed that the tractions on the two surfaces of a crack are equal and opposite.

Let $\mathbf{x}_p$ approach a point $\mathbf{y}_S$ on the uncracked boundary, we arrive at the following displacement boundary integral equation [3]:

$$b_{ij}u_j^t(\mathbf{y}_S) + \int_S T_{ij}^*(\mathbf{y}_S, \mathbf{x}_S)\, u_j^t(\mathbf{x}_S)\, \mathrm{d}S(\mathbf{x}_S) + \int_{\Gamma^+} T_{ij}^*(\mathbf{y}_S, \mathbf{x}_{\Gamma^+})\, [u_j^t(\mathbf{x}_{\Gamma^+}) - u_j^t(\mathbf{x}_{\Gamma^-})]\, \mathrm{d}\Gamma(\mathbf{x}_{\Gamma^+})$$

$$= \int_S U_{ij}^*(\mathbf{y}_S, \mathbf{x}_S)\, T_j^t(\mathbf{x}_S)\, \mathrm{d}S(\mathbf{x}_S) + \int_S T_{ij}^*(\mathbf{y}_S, \mathbf{x}_S)\, [u_j^p(\mathbf{x}_S) - u_i^p(\mathbf{y}_S)]\, \mathrm{d}S(\mathbf{x}_S)$$

$$- \int_S U_{ij}^*(\mathbf{y}_S, \mathbf{x}_S)\, T_j^p(\mathbf{x}_S)\, \mathrm{d}S(\mathbf{x}_S) \tag{3}$$

where b_{ij} are coefficients that depend only upon the local geometry of the uncracked boundary at $\mathbf{y}_S$. It is noteworthy that all the terms on the right-hand side of Equation (3) have only weak singularities, thus, are integrable. Although the second term on the left-hand side of Equation (3) has a strong singularity, it can be treated by the rigid-body motion method. At the same time, the calculation of b_{ij} can also be avoided.

A direct application of the standard or displacement boundary integral equation to fracture problems yields a mathematically degenerate formulation. In order to remedy this difficulty, the traction integral equation of Pan [3] can be employed and extended to a three-dimensional case. Assume that $\mathbf{y}_\Gamma$ is a smooth point on the crack surface, the traction integral equation can be derived as

$$[T_l^t(\mathbf{y}_{\Gamma^+}) - T_l^t(\mathbf{y}_{\Gamma^-})]/2 + n_m(\mathbf{y}_{\Gamma^+}) \int_S c_{lmik} T_{ij,k}^*(\mathbf{y}_{\Gamma^+}, \mathbf{x}_S) u_j^t(\mathbf{x}_S)\, \mathrm{d}S(\mathbf{x}_S)$$

$$+ n_m(\mathbf{y}_{\Gamma^+}) \int_\Gamma c_{lmik}\, T_{ij,k}^*(\mathbf{y}_{\Gamma^+}, \mathbf{x}_{\Gamma^+})\, [u_j^t(\mathbf{x}_{\Gamma^+}) - u_j^t(\mathbf{x}_{\Gamma^-})]\, \mathrm{d}\Gamma(\mathbf{x}_{\Gamma^+})$$

$$= [T_l^{\mathrm{p}}(\mathbf{y}_{\Gamma^+}) - T_l^{\mathrm{p}}(\mathbf{y}_{\Gamma^-})]/2 + n_m(\mathbf{y}_{\Gamma^+}) \int_S c_{lmik}\, U^*_{ij,k}(\mathbf{y}_{\Gamma^+}, \mathbf{x}_S)\, T^{\mathrm{t}}_j(\mathbf{x}_S)\, \mathrm{d}S(\mathbf{x}_S)$$

$$+ n_m(\mathbf{y}_{\Gamma^+}) \int_S c_{lmik}\, T^*_{ij,k}(\mathbf{y}_{\Gamma^+}, \mathbf{x}_S)\, u^{\mathrm{p}}_j(\mathbf{x}_S)\, \mathrm{d}S(\mathbf{x}_S)$$

$$- n_m(\mathbf{y}_{\Gamma_+}) \int_S c_{lmik}\, U^*_{ij,k}(\mathbf{y}_{\Gamma^+}, \mathbf{x}_S)\, T^{\mathrm{p}}_j(\mathbf{x}_S)\, \mathrm{d}S(\mathbf{x}_S) \tag{4}$$

where n_m is the unit outward normal of the positive side of the crack surface at $\mathbf{y}_{\Gamma^+}$ and c_{lmik} is the fourth-order stiffness tensor of the anisotropic medium; $U^*_{ij,k}$ and $T^*_{ij,k}$ are the derivatives of the Green's functions for displacements and tractions with respect to the source point respectively. Again these Green's functions are given exactly for a transversely isotropic solid with any oriented isotropic plane (see Appendix A) and explicitly for a generally anisotropic solid (see Appendix B).

Equations (3) and (4) form a pair of boundary integral equations and are similar to the single-domain BEMs of Mi and Aliabadi [10] for an isotropic medium. In this paper, however, the displacement integral equation is collocated exclusively on the uncracked boundary and the traction integral equation on one side of the crack surface only. Furthermore, this formulation can be applied to generally anisotropic media with the Cauchy-type integral being evaluated exactly by the rigid-body motion method. It is also worth mentioning that the effect of the body force and/or far-field stresses have been included by superposing the corresponding particular solution, which makes the problem very similar to the one associated with the homogeneous governing equations. The only difference is that for the body force and/or far-field stress cases, two extra integral terms related to the particular solution need to be added to the homogeneous integral equations. The advantage of using Equations (3) and (4) is that for the far-field stress case, the artificial truncation of the infinite domain or transferring of the far-field stress onto the problem boundary can be avoided. While the former method increases the size of the problem and also introduces errors because of the truncation of the region, the latter may not be suitable for the cases where the boundary has a complex shape. In the following analysis, the superscript t associated with the physical quantities will be omitted for simplicity, with the understanding that the physical quantities are the total ones.

For problems containing crack surfaces only, i.e. cracks in an infinite space, only Equation (4) is required with the uncracked boundary integral terms being omitted. The resulting equation resembles the displacement discontinuity method [6] and the dislocation method [14, 19, 20, 29]. For problems in an uncracked domain, only Equation (3) is required with the crack surface integral terms being omitted. Equation (3) is then reduced to the traditional displacement boundary integral equation [30].

The boundary integral equations (3) and (4) can be discretized and solved numerically for the unknown boundary displacements (or displacement discontinuities on the crack surface) and tractions. It is emphasized that in deriving Equation (4), we have assumed a smooth crack surface. If the crack surface possesses discontinuous tangential planes at certain points or along certain lines, discontinuous elements are required in which the collocation points are moved away from these points or lines. The hypersingular integral term in Equation (4) also requires special

attention and its handling by Kutt's [26, 27] numerical quadrature formulae will be discussed in a later section.

NUMERICAL SCHEME

Nine-node quadrilateral curved elements are employed to discretize both the uncracked boundaries and crack surfaces. On each element, the displacement and/or traction on the uncracked boundary, and the relative crack opening displacement (COD) on the crack surfaces can be approximated by their nodal values. For example, the total displacement on each element can be expressed as

$$u_i = \sum_{k=1}^{9} \phi_k u_i^k, \quad T_i = \sum_{k=1}^{9} \phi_k T_i^k, \quad \Delta u_i = \sum_{k=1}^{9} \phi_k \Delta u_i^k, \quad i = 1, 2, 3 \tag{5}$$

where ϕ_k ($k = 1$–9) are the shape functions, u_i^k, T_i^k, and Δu_i^l are the nodal displacements, nodal tractions, and nodal crack opening displacements at nodal point k and l, respectively.

In order to handle the possible discontinuities of the geometric and boundary conditions of the uncracked boundary and the crack surface, four and five types of nine-node quadrilateral elements are introduced respectively (Figures 2 and 3). It is noted that while element type I is continuous, others are discontinuous elements. The four sets of shape functions for the uncracked

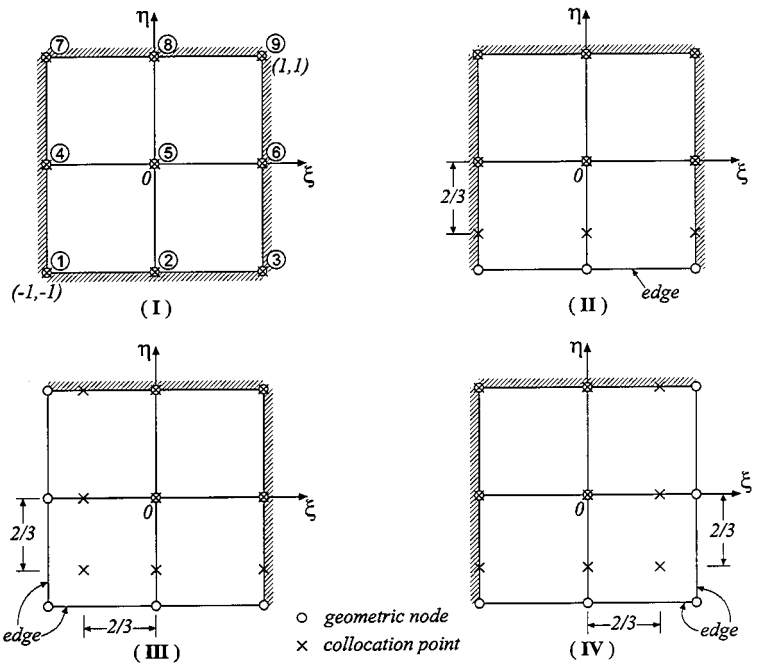

Figure 2. Four element types for the uncracked boundary.

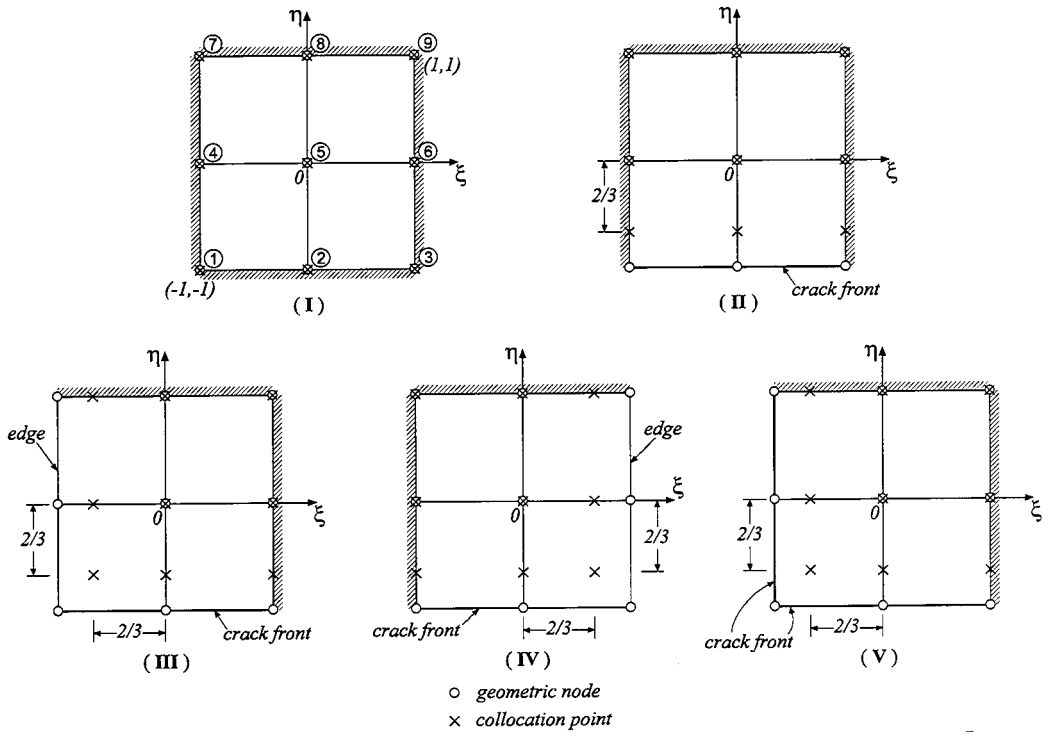

Figure 3. Five element types for the crack surface.

boundary are listed in Appendix C where the discontinuous nodes are at a distance of 1/3 from the element edge. Assuming isoparametric elements, the coordinates at any point in one element are then related to its element nodal co-ordinates as follows:

$$x = \sum_{k=1}^{9} \phi_k x_1^k, \quad y = \sum_{k=1}^{9} \phi_k x_2^k, \quad z = \sum_{k=1}^{9} \phi_k x_3^k \tag{6}$$

Furthermore, in order to capture the specific characteristics of the COD near a crack front, we constructed four sets of crack-front shape functions corresponding to the element type II–V shown in Figure 3. For crack-front element types II–IV, the following shape functions are introduced to approximate the COD

$$\Delta u_i = \sum_{k=1}^{9} (1+\eta)^{\delta+1} \varphi_k \Delta u_i^k \tag{7}$$

where δ is the order of the stress singularity near the crack front [31]; $\Delta u_i[= u_i(\mathbf{x}_{\Gamma^+}) - u_i(\mathbf{x}_{\Gamma^-})]$ are the CODs, φ_k ($k = 1$–9) are the nine shape functions which are similar to the corresponding shape functions for the uncracked boundary, except for the different coefficients for each shape function, and Δu_i^k are the CODs at nodal point k.

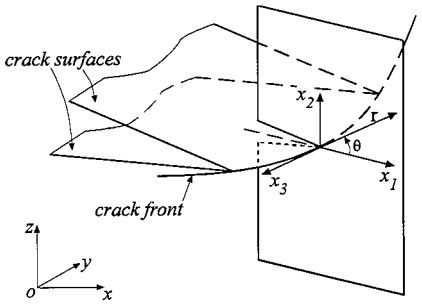

Figure 4. Geometric relation between local crack-front co-ordinates (x_1, x_2, x_3) and the global coordinates (x, y, z).

Similarly, on the crack-front element of type V, the COD is approximated as

$$\Delta u_i = \sum_{k=1}^{9} (1+\xi)^{\delta+1}(1+\eta)^{\delta+1}\varphi_k \Delta u_i^k \tag{8}$$

with φ_k ($k = 1$–9) being the shape functions corresponding to this type of element. Again, this set of shape functions is similar to the type III shape functions for the uncracked boundary.

When calculating the SIFs, we employ an extrapolation method of the CODs, which requires an asymptotically analytical expression of the crack-front CODs in terms of the SIFs. Let (x_1, x_2, x_3) be a local Cartesian co-ordinate system attached to the crack tip shown in Figure 4. The x_2-axis is normal to the crack surface, the x_3 tangential to the crack front. The x_1-axis is thus formed by the interaction of the plane normal to the crack front and the plane tangential to the crack plane. Suppose the crack front is smooth and the crack tip is away from the corner where the crack front meets a face on the uncracked boundary. It is assumed that the leading singular term in the asymptotic expansion of the stress and displacement fields near the crack tip is amenable to the generalized plane strain analysis. Therefore, for a crack tip in a homogeneous and anisotropic solid ($\delta = -1/2$), the relation of the CODs at a distance r behind the crack tip and the SIFs can be expressed as [31–34]

$$\Delta \mathbf{u} = 2\sqrt{\frac{2r}{\pi}}\,\mathbf{L}^{-1}\mathbf{k} \tag{9}$$

where $\mathbf{k} = (K_{\mathrm{II}}, K_{\mathrm{I}}, K_{\mathrm{III}})^{\mathrm{T}}$ are the stress intensity factors for modes I, II and III defined as

$$\begin{aligned} K_{\mathrm{I}} &= \lim_{r\to 0}\sqrt{2\pi r}\,\sigma_{22}(r,\theta,x_3)|_{\theta=0} \\ K_{\mathrm{II}} &= \lim_{r\to 0}\sqrt{2\pi r}\,\sigma_{12}(r,\theta,x_3)|_{\theta=0} \\ K_{\mathrm{III}} &= \lim_{r\to 0}\sqrt{2\pi r}\,\sigma_{23}(r,\theta,x_3)|_{\theta=0} \end{aligned} \tag{10}$$

Expression (9) is based on Stroh formalism. **L** is one of the Barnett–Lothe tensors which depends only on the anisotropic properties of the solid in the local crack-front co-ordinates, and $\Delta\mathbf{u} = [\Delta u_1, \Delta u_2, \Delta u_3]^{\mathrm{T}}$ is the COD in the local crack-front co-ordinates. On the crack-front element, equating the CODs from the numerical calculation (7) or (8) to the analytical expression (9), one then obtains a set of algebraic equations from which the SIFs, K_{I}, K_{II}, and K_{III}, can be solved.

TREATMENT OF HYPERSINGULAR INTEGRAL EQUATIONS

In solving the pairs of boundary integral Equations (3) and (4), special attention needs to be paid to the singular terms involved. As mentioned earlier, the Cauchy-type singularity in Equation (3) can be directly evaluated by the rigid-body motion method. For the finite-part integrals in Equation (4), a Kutt's [26, 27] numerical quadrature is proposed to solve the hypersingular integral equations.

On each isoparametric element, the finite-part integral can be expressed as

$$\int_{-1}^{1}\int_{-1}^{1} F[\mathbf{y}(\xi^{\mathrm{c}}, \eta^{\mathrm{c}}), \mathbf{x}(\xi, \eta)]\, \phi_k(\xi, \eta)\, g(\xi, \eta)\, J(\xi, \eta)\, \mathrm{d}\xi\, \mathrm{d}\eta \tag{11}$$

with

$$g(\xi,\eta) = \begin{cases} 1 & \text{for interior elements} \\ (1+\eta)^{\delta+1} & \text{for crack-front element types II–IV} \\ (1+\xi)^{\delta+1}(1+\eta)^{\delta+1} & \text{for crack-front element type V} \end{cases} \tag{12}$$

Also in Equation (11), $F \propto O(1/r^3)$ represents one component of $n_m c_{lmik} T^{*}_{ij,k}\, u_j$, ϕ_k are the shape functions and J is the Jacobian transformation. The collocation point $\mathbf{x}(\xi^c, \eta^c)$ in Equation (11) coincides with one of the nodal points on the element.

Introducing the following polar coordinates transform

$$\begin{aligned} \xi &= \xi^{\mathrm{c}} + r\cos\theta \\ \eta &= \eta^{\mathrm{c}} + r\sin\theta \end{aligned} \tag{13}$$

Equation (11) can then be rewritten as

$$\sum_m \int_{\theta_1}^{\theta_2}\int_0^{R(\theta)} F[\mathbf{y}(\xi^{\mathrm{c}}, \eta^{\mathrm{c}}), \mathbf{x}(r, \theta)]\, \phi_k(r, \theta)\, g(r, \theta)\, J(r, \theta)\, r\, \mathrm{d}r\, \mathrm{d}\theta \tag{14}$$

where the summation on m is for all the triangles needed on the element. For instance, if the collocation point is one of the corner points of the element, the element is then divided into two triangles, and the summation on m is from 1 to 2. On the other hand, if the collocation point is an internal point, the element needs to be divided into four triangles. Consequently, the summation on m in Equation (14) is from 1 to 4. It is observed now that the integrand is $O(1/r^2)$. Therefore,

Kutt's [26, 27] numerical quadrature can be utilized to evaluate the inner finite-part integral with respect to r. The outer integral with respect to θ is regular and can be calculated by the regular Gauss quadrature.

For a given Gauss point θ_j, the inner integral in Equation (14) can be approximated by Kutt's N-point equispace quadrature as

$$\int_0^R \frac{f(r)}{r^2}\,\mathrm{d}r \approx \frac{1}{R}\sum_{i=1}^{N}(w_i + c_i \ln R) f\left(\frac{i-1}{N}R\right) \tag{15}$$

where w_i are the weights and c_i the coefficients given by Kutt, and the integrand is given by

$$f(r) = F[\mathbf{y}(\xi^c, \eta^c), \mathbf{x}(r, \theta_j)]\,\phi_k(r, \theta_j)\,g(r, \theta_j)\,J(r, \theta_j)\,r^3 \tag{16}$$

In applying Kutt's N-point equispace quadrature (15), it has been assumed that the integrand $f(r) \in C^0[0, R]$ and $f(r) \in C^2$ in the neighbourhood of $r = 0$ [26, 27]. Therefore, if the crack surface is flat, continuous elements can be used to discretize the interior crack surface, with discontinuous elements for the crack-fronts only. However, if the crack surface is curved, then discontinuous elements are needed for the whole crack surface in order to satisfy the continuity requirement for $f(r)$. In the following numerical examples, Kutt's 20-point equispace quadrature is used to the finite-part integral with respect to r, and 20 Guassian points for the regular outer integral with respect to θ. Since we restrict ourselves in this paper to the flat crack surfaces only, continuous elements are used to discretize the interior crack surface.

NUMERICAL RESULTS AND DISCUSSION

The Green's functions for transversely isotropic solids with arbitrarily oriented isotropic plane [28, 35] and for generally anisotropic solids [36] have been incorporated into the displacement and traction integral equations, and the resulting formulation has been programmed for numerical calculation. In this section, several numerical examples including the solids with infinite domain and finite geometry are presented to verify the program and to show the efficiency and accuracy of the present BEM formulation in calculating the SIFs in transversely isotropic and anisotropic media. In all the examples, a uniaxial normal stress is applied normal to the crack surface. The effects of material anisotropy, material orientation, crack geometry and finite geometry on the SIFs are demonstrated. Numerical results also show that material anisotropy can have a profound effect on the SIFs.

Example 1: A penny-shaped crack in an infinite space

The first example considers a penny-shaped crack (with radius $a = 5$ in.) located in the x–y plane in an infinite space under a far-field uniform stress σ^∞ applied in the z-direction. Forty-eight nine-node quadrilateral elements are used to discretize the crack surface (Figure 5). Geometric nodes and collocation points are also shown in the figure. For the isotropic solid ($E = 4$ Msi and $\nu = 0.25$ are used in modelling), the normalized mode-I stress intensity factor, $K_\mathrm{I}/(2\sigma^\infty\sqrt{a/\pi})$, along the crack front varies from 0.99 to 1.01, compared with the value of unity in the analytical

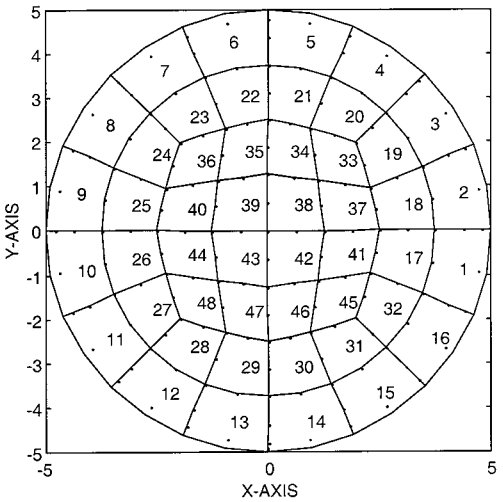

Figure 5. Discretization of a penny-shaped crack (radius $a = 5$ in.) with 48 nine-node quadrilateral elements.

solution $K_I^{\text{ref}} = 2\sigma^{\infty}\sqrt{a/\pi}$ [37]. The largest deviation for the SIFs using the 3D BEM formulation is only about 1 per cent, even with only 48 elements modelled in the crack region (16 elements along the crack front). It is noted that for the penny-shaped or elliptical crack, [37] the mode-I SIF in an infinite isotropic solid is independent of the material property.

Two classes of transversely isotropic (TI) solids are then selected to study the effect of material anisotropy on the SIFs.

For class I material, $E_X/E_Z = 3$, $\nu_{XY} = 0.25$, $\nu_{YZ} = 0.25$ and $G_{YZ}/E_Z = 0.4$
For class II material, $E_X/E_Z = 0.5$, $\nu_{XY} = 0$, $\nu_{YZ} = 0.4$ and $G_{YZ}/E_Z = 0.8$

The material properties for classes I and II are chosen from the papers by Pan and Amadei, [11] and Hoenig, [23] respectively. X, Y and Z refer to longitudinal, transverse and normal direction respectively. (X, Y, Z) are often called principal material axes and the plane X–Y is termed as principal material plane of the plane of isotropy in this case. In the transversely isotropic solids, $E_X = E_Y$, $G_{XZ} = G_{YZ}$, $\nu_{XZ} = \nu_{YZ}$, and $G_{XY} = E_X/2(1 + \nu_{XY})$. ν_{XY} is the Poisson's ratio for transverse strain in the Y-direction when stressed in the X-direction (Figure 6).

For the plane of isotropy parallel to the penny-shaped crack surface (x–y plane), TI-0, the 3-D BEM results also predict a nearly constant SIF close to the analytical solution, $K_I^{\text{ref}} = 2\sigma^{\infty}\sqrt{a/\pi}$, along the crack front (Figure 7). However, for the plane of isotropy not parallel to the crack surface, TI-90, the SIFs then vary along the crack front. In the case of the orientation angle $\beta = 90^{\circ}$ and inclination angle $\psi = 90^{\circ}$ (Figure 6), which corresponds to the plane of isotropy being normal to the crack plane (or parallel to the space fixed x–z plane), the crack is under pure mode-I subjected to a remote uniform stress σ^{∞} in the z-direction. The variation of K_{I} along the crack front is also shown in Figure 7 for the two classes of transversely isotropic solids. It is interesting to note from Figure 7 that the variation of the SIF for class II is similar (but not the

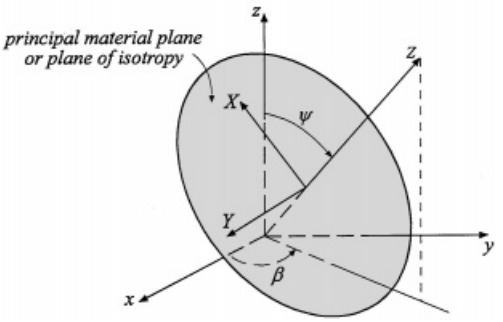

Figure 6. Relationship between the principal material co-ordinates (X, Y, Z) and the space-fixed global coordinates (x, y, z). β and ψ are the orientation and inclined angles, respectively. (X, Y) is the principal material plane or plane of isotropy.

same!) to that obtained by Hoenig [23]; variation of the SIF for classes I and II material follows a function

$$A_i + B_i \cos 2\theta, \quad i = \text{I or II} \tag{17}$$

where θ is measured counterclockwise from the x-axis. Due to the different material anisotropy ratio, E_X/E_Z, between these two materials, the maximum (minimum) values of K_I for class I occur at $\theta = 90$ and 270° (0 and 180°) respectively; reverse trend for class II.

Example 2: A square-shaped crack in an infinite space

A square-shaped crack in the x–y plane in an infinite space is studied in this example. The side length of the square is $2a$ ($= 6$ in.), and a far-field stress σ^∞ is applied in the z-direction. The square-shaped crack can be seen in Figure 13 which will be discussed in the next example. One hundred (10×10) nine-node quadrilateral elements are used to discretize the square with the meshes shown in Figure 8. To gain an insight into the stress intensity factors affected by the material anisotropy, two sets of material properties, transversely isotropic and anisotropic materials, are studied for this shape of the crack. The first set of numerical results utilizes a transversely isotropic (TI) material whose material properties are the same as the class I in Example 1. Three material orientations for the transversely isotropic material under normal loading are studied: (i) TI-0 corresponds to the plane of isotropy parallel to the crack surface; (ii) TI-90 represents the plane of isotropy normal to the crack surface ($\beta = 90^\circ$ and $\psi = 90^0$), respectively; and (iii) TI-45 corresponds to $\beta = 45^\circ$ and $\psi = 45^\circ$ where the stiffness matrix is fully populated. The normalized SIFs, $K_\text{I}/(\sigma^\infty\sqrt{\pi a})$, along $x = \pm a$ and $y = \pm a$ for three material orientations are shown in Figure 9.

The variation of mode-I SIFs along the crack front for TI-0 either along $x = \pm a$ or $y = \pm a$ is shown in Figure 9. For comparison, the SIFs for isotropic materials are also calculated and shown in the figure. Note that for either a penny-shaped or an elliptical crack with crack plane parallel to the plane of isotropy in an infinite space, the analytical forms for the mode-I stress intensity factor [22, 23] are independent of material properties. In this case of a square-shaped crack in an infinite space, the variation of mode-I SIFs along the crack front for the TI-0 shown in

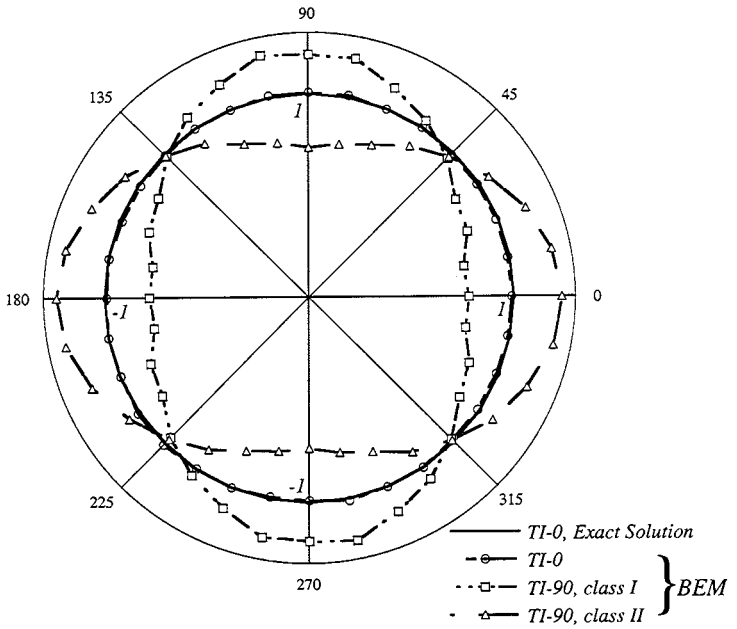

Figure 7. Variation of $K_I/(2\sigma^{\infty}\sqrt{a/\pi})$ along the penny-shaped crack front of transversely isotropic solids (TI-0 and TI-90) in an infinite space under a far-field normal stress σ^{∞}.

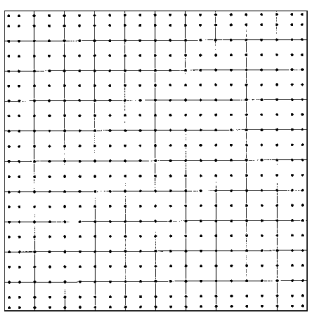

Figure 8. Discretization of a square-shaped crack (side length $2a = 6$ in.) with 100 nine-node quadrilateral elements.

Figure 9, as expected, is the same as that for the isotropic case, i.e. independent of material properties. The values are almost the same as that obtained by Weaver using a dislocation method. The maximum value occurs at the middle of the square side and decrease to zero at the corners ($x = \pm a$, $y = \pm a$). The maximum SIF value that predicted from the 3-D BEM is 0.7626, as compared with 0.74 in Weaver [38] and 0.76 in Murakami [39] for isotropic solids.

The effect of material anisotropy on mode-I SIFs can be demonstrated in the TI-90 case. In this case, the mode-I SIF along the crack front $y = \pm a$ is much larger than that along $x = \pm a$, about

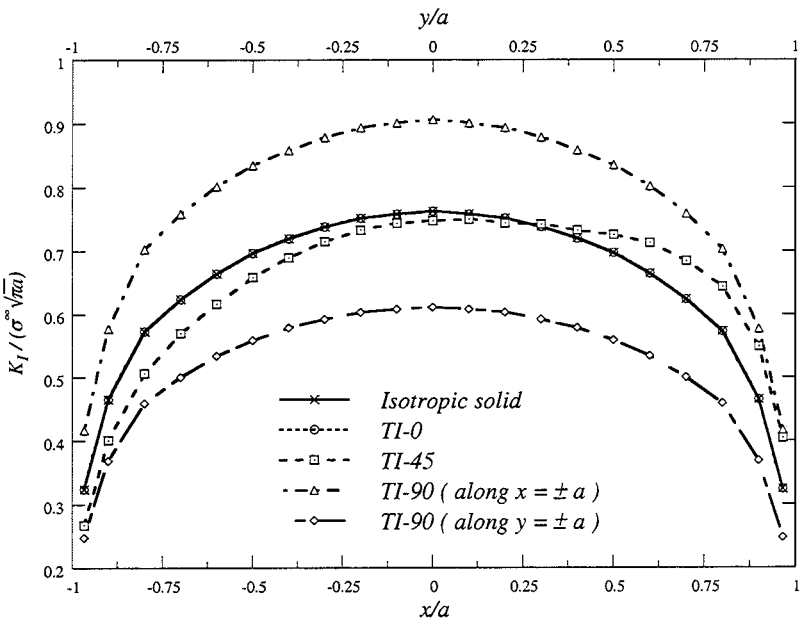

Figure 9. Variation of $K_I/(\sigma^\infty\sqrt{\pi a})$ along the square-shaped crack front of a transversely isotropic solid in an infinite space under a far-field normal stress σ^∞.

30 per cent greater when compared with their maximum values. It is also expected that the SIFs for the cases of isotropic, TI-0 and TI-90 materials are symmetrical about $x = 0$ and $y = 0$, the SIFs for TI-45 also shown in Figure 9 are unsymmetric with respect to either $x = 0$ or $y = 0$. Due to the material orientation for TI-45, the mode-I SIFs along the crack front $y = \pm a$ are the same as those along $x = \pm a$. In addition, the fracture exhibits mixed mode-I, II and III behaviour. The variation of mode-II and III stress intensity factors along the crack front $x = -a$ is shown in Figure 10. In this figure, the maximum absolute value of mode-II SIF is about 15 per cent of the maximum value for mode-I SIF. The values of K_{II} and K_{III} follow the relations

$$K_{II}(x = a, y) = -K_{II}(x = -a, y), \quad K_{III}(x = a, y) = -K_{III}(x = -a, y)$$
$$K_{II}(x, y = -a) = K_{II}(x = -a, y), \quad K_{III}(x, y = -a) = -K_{III}(x = -a, y)$$
$$K_{II}(x, y = a) = -K_{II}(x, y = -a), \quad K_{III}(x, y = a) = -K_{III}(x, y = -a)$$

It is emphasized at this point that in the procedure of deriving the BEM formulation, no assumption has been made regarding the material anisotropy. Therefore, the present formulation can be equally well applied to either orthotropic or general anisotropic solids. The only difference in the numerical calculation is the Green's functions. For a transversely isotropic solid with any oriented isotropic plane, these Green's functions are given in exact-closed forms (Appendix A). However, for either orthotropic or general anisotropic solids, they can only be evaluated explicitly through a sixth-order polynomial (Appendix B).

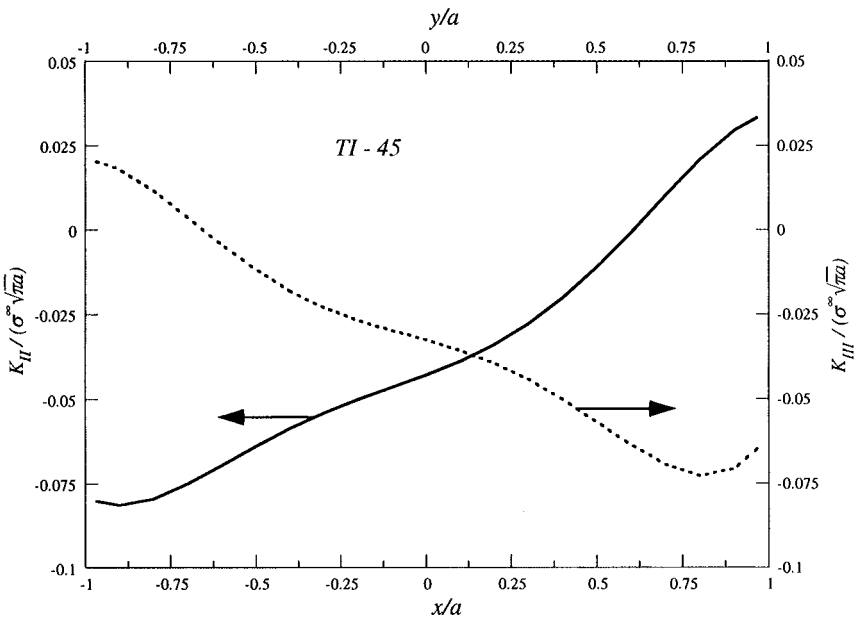

Figure 10. Variation of $K_{II}/(\sigma^{\infty}\sqrt{\pi a})$ and $K_{III}/(\sigma^{\infty}\sqrt{\pi a})$ along the square crack front $x = -a$ of a transversely isotropic solid in an infinite space under a far-field normal stress σ^{∞}.

Another set of numerical results is investigated for anisotropic solids (or composites). The composite material was made by stacking layers of a carbon warp-knit fabric that was stitched with Kevlar-29 thread prior to introducing 3501-6 epoxy resin. The resin was introduced in an autoclave using a resin film infusing process. In the NASA Advanced Composites Transport Program, Boeing is using this material to develop a composite wing box for a transport aircraft. The fibre areal weight of each fabric layer was equivalent to 10 layers of 145 g/m^2 prepreg. The fabric contained 44 per cent 0° yarns, 44 per cent $\pm 45°$ yarns, and 12 per cent 90° yarns. The resulting orthotropic material properties are:

$$E_X = 11.773 \text{ Msi}, \quad E_Y = 5.162 \text{ Msi}, \quad E_Z = 1.53 \text{ Msi},$$

$$G_{XY} = 2.479 \text{ Msi}, \quad G_{XZ} = 0.64 \text{ Msi}, \quad G_{YZ} = 0.57 \text{ Msi},$$

$$\nu_{XY} = 0.401, \qquad \nu_{XZ} = 0.22, \qquad \nu_{YZ} = 0.29$$

Three different material orientations are studied, For class I (orthotropic material), E_X, E_Y, and E_Z are along the z, x and y-axis, respectively ($\beta = -90°$ and $\psi = 90°$); for class II, E_X and E_Y are in the x–y plane respectively, and E_X is rotated 45° counterclockwise with respect to the x-axis ($\beta = 45°$ and $\psi = 0°$). In this case, the stiffness tensor c_{ijkl} in the structural co-ordinates (x, y, z) is monoclinic with symmetry plane at $z = 0$. In the class III material, E_X and E_Y are in the x–z plane, and E_X is rotated 45° counterclockwise with respect to the x-axis. The global elastic property for

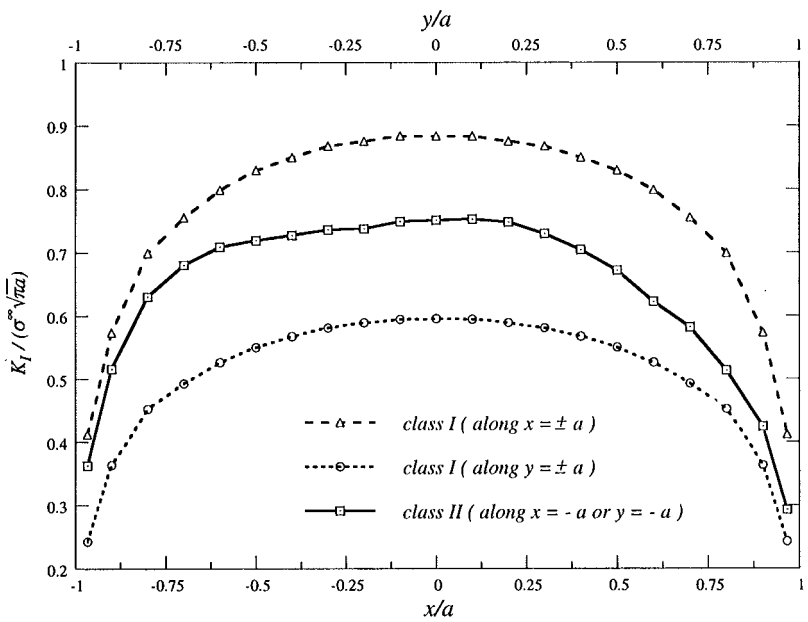

Figure 11. Variation of $K_I/(\sigma^\infty\sqrt{\pi a})$ along the square-shaped crack front of anisotropic solids in an infinite space under a far-field normal stress σ^∞.

the class III is monoclinic having symmetry plane at $y = 0$. This material orientation simulates an off-axis composite.

For the same square-shaped crack but in anisotropic solids, the anisotropic Green's functions are calculated accurately in Appendix B. The normalized SIFs, $K_I/(\sigma^\infty\sqrt{\pi a})$, along the crack fronts are shown in Figure 11 for classes I and II. It is worth mentioning that under remote normal stress $\sigma_z = \sigma^\infty$ the crack is pure mode-I for class I. The variation of mode-I SIFs along the rack front for class I (i.e. the orthotropic case) is, however, different from that for the isotropic or the TI-0 case in the infinite space shown in Figure 9. For the orthotropic case, the maximum values of the mode-I SIF along $x = \pm a$ and $y = \pm a$ are, respectively, 0.5953 and 0.8833, compared to 0.7626 for the isotropic or the TI-0 case. For class II where $z = 0$ is the material symmetry plane, the problem is also under pure mode-I deformation, but the SIF values are unsymmetric on either $y = 0$ or $x = 0$. The SIFs are symmetric with respect to $x = y$. The SIFs along $x = -a$ or $y = -a$ are also shown in Figure 11.

For class III where $y = 0$ is the material symmetry plane, however, the fracture exhibits mixed mode-I, II and III behaviour. The mode-I SIFs along the crack front $x = \pm a$ are much larger than those along $y = \pm a$. They are symmetric with respect to $x = 0$ and $y = 0$. The corresponding variations of mode-II and III SIFs along the crack front $x = -a$ and $y = -a$ for class III are shown in Figure 12. The mode-II SIF values are anti-symmetric about $x = 0$ and symmetric about $y = 0$. For mode-III SIF values, they are symmetric about $x = 0$ and anti-symmetric about $y = 0$. While these SIF values have the same order of magnitude, their maximum absolute values are less than 10 per cent of the maximum values for the corresponding mode-I SIFs.

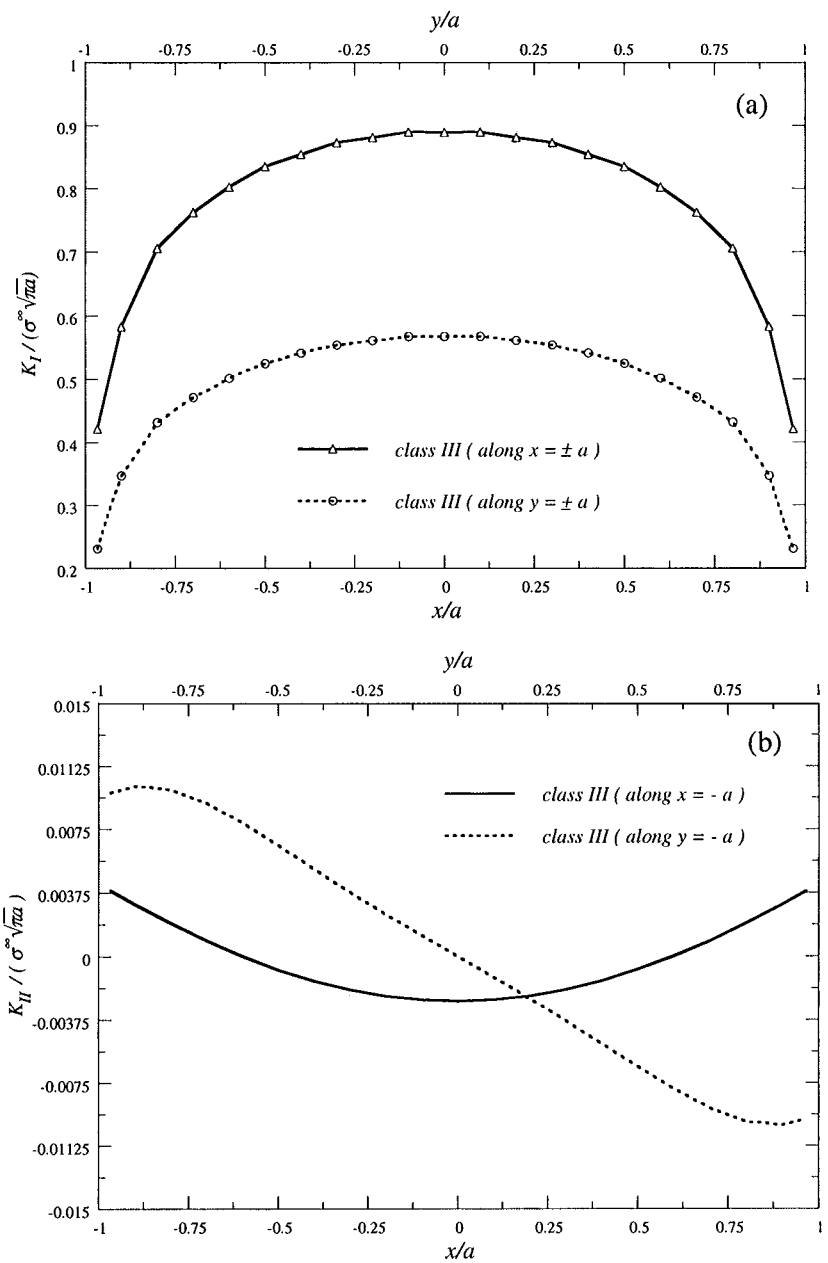

Figure 12. Variation of $K_I/(\sigma^\infty\sqrt{\pi c})$, $K_{II}/(\sigma^\infty\sqrt{\pi a})$ and $K_{III}/(\sigma^\infty\sqrt{\pi a})$ along the square crack front of an anisotropic solid in an infinite space under a far-field normal stress σ^∞.

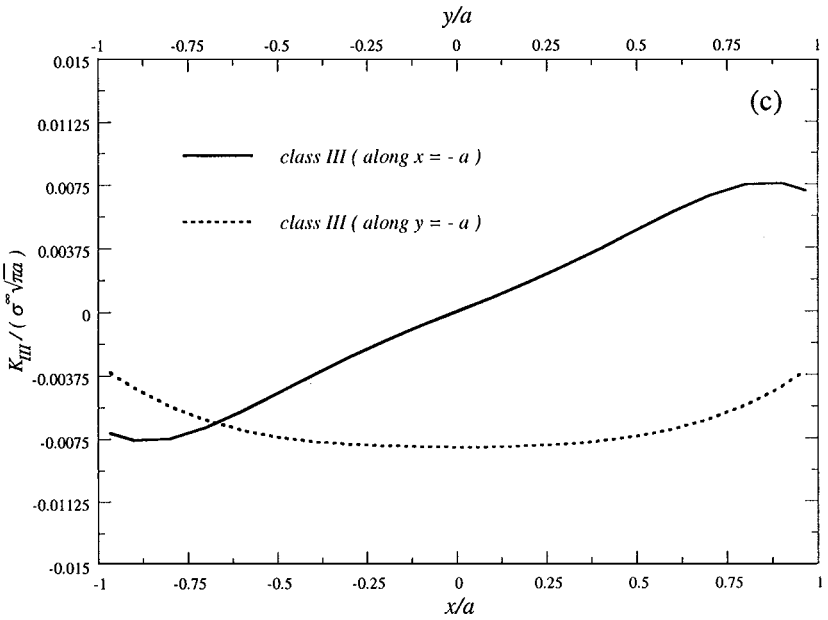

Figure 12. *Continued.*

Example 3: A square-shaped crack in a finite cube

To study the effect of finite geometry on the SIFs, a square-shaped crack in a finite cube under a uniform tensile stress σ^{∞} applied at the top and bottom faces in the z-direction (Figure 13) is studied. The cube has a height $2H$ and a width W. The side length of the square crack is $2a$. In the numerical example, the geometry is such that $2a/W = 0.5$, $H/W = 1$, and the material is assumed to be isotropic with $E = 4$ Msi and $v = 0.3$. Twenty-four and 36 elements are used to discretize, respectively, the uncracked boundary and the crack surface. It is noted that, while for Examples 1 and 2, only Equation (4), with the uncracked boundary integral being discarded is needed. For this example, however, both Equations (3) and (4) are required to model the problem. The normalized mode-I SIF along the y-axis is shown in Figure 14 and compared with that in the corresponding infinite medium. As expected, the normalized SIF value is larger in a finite cube than that in an infinite domain, with a maximum difference of 6.8 per cent occurring at the middle of the square side for the chosen geometry and material property. Also in the middle of the square side, the normalized SIF in the finite cube is 0.8183, as compared to about 0.81 from a paper by Wen and Aliabadi [40] for the same geometry.

CONCLUSIONS

A single-domain three-dimensional BEM formulation has been proposed for fracture mechanics analysis in anisotropic elastic cracked media. The formulation consists of a pair of integral

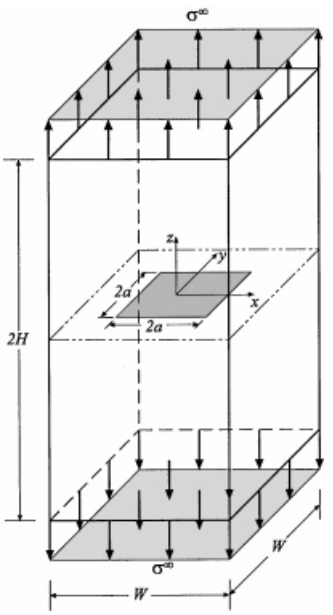

Figure 13. Geometry of a finite cube with a central square-shaped crack under a uniform normal stress σ^{∞}.

equations, namely, the displacement and traction integral equations. While the Cauchy-type singularity was calculated directly by the rigid-body motion method, the finite-part integral was evaluated by Kutt's numerical quadrature. Special crack-front elements have been introduced to capture the crack-tip behaviour of the crack opening displacement, and an extrapolation method of the COD is employed for the calculation of the stress intensity factors.

Numerical examples of the calculation of the SIFs for a penny-shaped and a square-shaped crack in transversely isotropic, orthotropic and anisotropic solids were conducted. The effects of material anisotropy, material orientation, crack geometry and finite geometry on the SIFs have been demonstrated. The SIF values are in very good agreement with previously published results. Material anisotropy can have a significant effect on the SIFs. It is the authors' belief that the single-domain BEM formulation presented in this paper can be a powerful numerical tool, which can apply to various complex three-dimensional geometries of composite structures with cracks or damage under mixed-mode loading. Some of the related problems are currently under investigation by the authors and results will be published in a separate paper.

APPENDIX A: GREEN'S FUNCTIONS IN TRANSVERSELY ISOTROPIC SOLIDS

In this appendix, the Green's functions in a transversely isotropic solid with any oriented isotropic plane are presented based on the results of Pan and Chou [35] and Pan and Amadei [28].

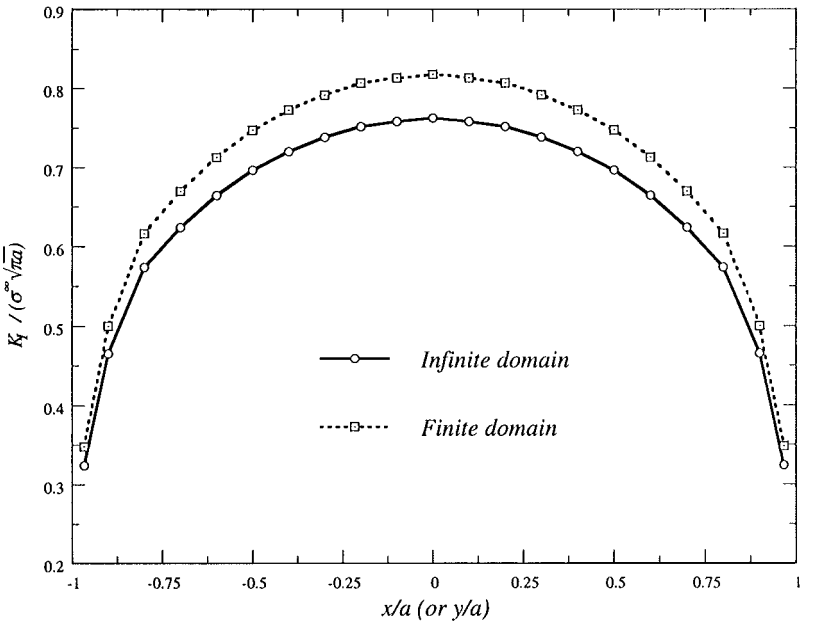

Figure 14. Comparison of $K_I/(\sigma^\infty\sqrt{\pi a})$ along the square-shaped crack front in an infinite domain and a finite cube.

For a transversely isotropic solid with the Z-axis being the axis of material symmetry, X–Y plane is the plane of isotropy. The constitutive relation between the stress σ_{ij} and strain ε_{ij} can be expressed in terms of contracted stiffness matrix as

$$\begin{bmatrix} \sigma_{XX} \\ \sigma_{YY} \\ \sigma_{ZZ} \\ \sigma_{YZ} \\ \sigma_{XZ} \\ \sigma_{XY} \end{bmatrix} = \begin{bmatrix} c_{11} & c_{12} & c_{13} & 0 & 0 & 0 \\ & c_{11} & c_{13} & 0 & 0 & 0 \\ & & c_{33} & 0 & 0 & 0 \\ & & & c_{44} & 0 & 0 \\ & \textit{Symmetric} & & & c_{44} & 0 \\ & & & & & c_{66} \end{bmatrix} \begin{bmatrix} \varepsilon_{XX} \\ \varepsilon_{YY} \\ \varepsilon_{ZZ} \\ 2\varepsilon_{YZ} \\ 2\varepsilon_{XZ} \\ 2\varepsilon_{XY} \end{bmatrix} \tag{A1}$$

where $c_{66} = (c_{11} - c_{12})/2$. Assuming that there is a unit point force applied at the origin of the co-ordinate system, the corresponding Green's displacements have been obtained by Pan and Chou [35] using the potential function method.

(i) For a point force applied at the origin in the Z-direction, the Green's displacements are

$$U^*_{XZ}(X, Y, Z) = \sum_{i=1}^{2} \left[v_i A_i \frac{X}{R_i R_i^*} - v_i (A_i + B_i) \frac{XZ_i}{R_i^3} \right]$$
$$U^*_{YZ}(X, Y, Z) = U^*_{XZ}(Y, X, Z) \tag{A2}$$

$$U^*_{ZZ}(X, Y, Z) = -\sum_{i=1}^{2}\left[\left(\frac{c_{11}B_i + c_{44}v_i^2 A_i}{c_{13} + c_{44}}\right)\frac{1}{R_i} + \frac{(A_i + B_i)v_i^2}{c_{13} + c_{44}}\frac{c_{44}(X^2 + Y^2) + c_{11}Z^2}{R_i^3}\right] \quad \text{(A2)}$$

where $U^*_{ij}(X, Y, Z)$ is the Green's function for displacement in the i-direction at the field point (X, Y, Z) caused by a point force in the j-direction applied at the origin (0, 0, 0), i.e. the source point. In Equation (A2)

$$\begin{aligned} R_i^* &= R_i + Z_i \\ R_i &= \sqrt{X^2 + Y^2 + Z_i^2} \\ Z_i &= v_i Z \end{aligned} \quad \text{(A3)}$$

and the constants A_i and B_i are determined as

$$v_1 A_1 = -v_2 A_2 = \frac{c_{13} + c_{44}}{4\pi c_{33}c_{44}(v_2^2 - v_1^2)} \quad \text{if } \sqrt{c_{11}c_{33}} - c_{13} - 2c_{44} \neq 0 \quad \text{(A4)}$$

$$\begin{aligned} B_i &= -A_i \\ A_1 &= A_2 = 0 \end{aligned}$$

$$B_1 = B_2 = -\frac{c_{13} + c_{44}}{16\pi c_{11}c_{44}}, \quad \text{if } \sqrt{c_{11}c_{33}} - c_{13} - 2c_{44} = 0 \quad \text{(A5)}$$

In Equations (A2)–(A5), the parameters v_i are related to the elastic constants c_{ij} as

$$\begin{aligned} v_3 &= \sqrt{c_{66}/c_{44}} \\ v_1 &= \sqrt{a} + \sqrt{b} \\ v_2 &= \sqrt{a} - \sqrt{b} \end{aligned} \quad \text{(A6)}$$

with

$$\begin{aligned} a &= \frac{(\sqrt{c_{11}c_{33}} - c_{13})(\sqrt{c_{11}c_{33}} + c_{13} + 2c_{44})}{4c_{33}c_{44}} \\ b &= \frac{(\sqrt{c_{11}c_{33}} + c_{13})(\sqrt{c_{11}c_{33}} - c_{13} - 2c_{44})}{4c_{33}c_{44}} \end{aligned} \quad \text{(A7)}$$

(ii) For a point force applied at the origin in the X-direction, the Green's function for displacements are

$$\begin{aligned} U^*_{XX}(X, Y, Z) &= \sum_{i=1}^{2}\left[(A_i' - B_i')\left(\frac{v_i}{R_i} - \frac{v_i X^2}{R_i^3}\right) + 2v_i B_i'\left(\frac{1}{R_i^*} - \frac{X^2}{R_i R_i^{*2}}\right)\right] + D\left(\frac{1}{R_3^*} - \frac{Y^2}{R_3 R_3^{*2}}\right) \\ U^*_{YX}(X, Y, Z) &= -\sum_{i=1}^{2}\left[v_i(A_i' - B_i')\frac{XY}{R_i^3} + 2v_i B_i'\frac{XY}{R_i R_i^{*2}}\right] + D\frac{XY}{R_3 R_3^{*2}} \\ U^*_{ZX}(X, Y, Z) &= -\sum_{i=1}^{2}\left[v_i^2 k_i(A_i' - B_i')\frac{XZ_i}{R_i^3} + \frac{c_{11}A_i' - c_{44}v_i^2 B_i'}{c_{13} + c_{44}}\frac{2X}{R_3 R_3^*}\right] \end{aligned} \quad \text{(A8)}$$

where

$$k_i = \frac{c_{11}/v_i^2 - c_{44}}{c_{13} + c_{44}}$$
$$D = \frac{1}{4\pi c_{44} v_3} \tag{A9}$$

and A_i' and B_i' are obtained as

$$A_1' = B_1' = -\frac{c_{44} - c_{33}v_1^2}{8\pi c_{33}c_{44}(v_1^2 - v_2^2)v_1^2}$$
$$A_2' = B_2' = \frac{c_{44} - c_{33}v_2^2}{8\pi c_{33}c_{44}(v_1^2 - v_2^2)v_2^2} \quad \text{if } \sqrt{c_{11}c_{33}} - c_{13} - 2c_{44} \neq 0 \tag{A10}$$

$$A_1' = A_2' = \frac{1}{16\pi c_{11}}$$
$$B'_1 = B_2' = \frac{1}{16\pi c_{44}v_1^2} \quad \text{if } \sqrt{c_{11}c_{33}} - c_{13} - 2c_{44} = 0 \tag{A11}$$

(iii) For a point force applied at the origin in the Y-direction, the Greens function for displacement can be obtained by interchanging X and Y in equation (A9), i.e.

$$U_{XY}^*(X, Y, Z) = U_{YX}^*(Y, X, Z)$$
$$U_{YY}^*(X, Y, Z) = U_{XX}^*(Y, X, Z) \tag{A12}$$
$$U_{ZY}^*(X, Y, Z) = U_{ZX}^*(Y, X, Z)$$

With these Green's functions being known exactly, their derivatives with respect to either a source or field point can be directly carried out. For Green's functions in an infinite space, as for the current case here, their derivatives with respect to a source point are opposite to those with respect to the corresponding field point.

It is observed clearly from the definition of R_i^* (i.e. Equation (A3)) that for field points (X, Y, Z) located on the negative Z-axis, the above Green's functions breakdown. In such a case, Green's functions at the image point are calculated and imaged back to those corresponding to the field point on the negative Z-axis.

The above Green's functions are valid only in a principal material co-ordinate with the Z-axis being the axis of elastic symmetry. For an infinite solid of transverse isotropy with arbitrarily oriented isotropic plane, the Green's functions expressed in terms of the local co-ordinates (X, Y, Z) need to be transformed to the global co-ordinates (x, y, z). The relationship of the global (x, y, z) and local (X, Y, Z) co-ordinate systems is illustrated in Figure 6, i.e.

$$\begin{bmatrix} x \\ y \\ z \end{bmatrix} = \mathbf{H} \begin{bmatrix} X \\ Y \\ Z \end{bmatrix} \tag{A13}$$

where the elements of matrix **H** are

$$\mathbf{H} = \begin{bmatrix} -\cos\psi\cos\beta & \sin\beta & \sin\psi\cos\beta \\ -\cos\psi\sin\beta & -\cos\beta & \sin\psi\sin\beta \\ \sin\psi & 0 & \cos\psi \end{bmatrix} \tag{A14}$$

With the co-ordinate transformation matrix **H**, the Green's functions for displacements, U_{ij}^*, in terms of global co-ordinates can be obtained as

$$\mathbf{U}_{\text{global}}^* = \mathbf{H}\mathbf{U}_{\text{local}}^*\mathbf{H}^{\mathrm{T}} \tag{A15}$$

The Green's functions for tractions, T_{ij}^*, can be derived in a similar procedure.

APPENDIX B: GREEN'S FUNCTIONS IN ANISOTROPIC SOLIDS

The Green's functions in an anisotropic infinite space have been derived recently by Tonon *et al.* [36] based on the theory of the residues. Here we outline only the displacements Green's functions. Assuming that there is a unit point force applied at the origin in the *j*-direction, the Green's function for displacement in the *i*-direction at the field point **x** can be expressed in terms of the following integral:

$$U_{ij}^*(\mathbf{x}) = \frac{1}{8\pi^2}\int_{\Omega} \Gamma_{ij}^{-1}(\mathbf{n})\,\delta(\mathbf{n}\cdot\mathbf{x})\,\mathrm{d}\Omega(\mathbf{n}) \tag{B1}$$

where Ω is any closed surface in a three-dimensional **n**-space which encloses the origin point $\mathbf{n} = 0$. $D(\mathbf{x})$ is the delta function, and

$$\Gamma_{ij}^{-1}(\mathbf{n}) = (c_{ikjl}\,n_k\,n_l)^{-1} \tag{B2}$$

with c_{ikjl} being the stiffness tensor of the anisotropic solid. It was shown in Tonon *et al.* [36] that Equation (B1) can be reduced to an one-dimensional infinite integral with the latter integral being evaluated by the theory of the residues. Therefore, the Green's functions for displacement (B1) can be obtained as

$$U_{ij}^*(\mathbf{x}) = -\frac{1}{2\pi r}\,\mathrm{Im}\left[\sum_{m=1}^{3} \frac{A_{ij}(\mathbf{p}+\zeta_m\mathbf{q})}{a_7(\zeta_m-\bar{\zeta}_m)\prod\limits_{\substack{k=1\\k\neq m}}^{3}(\zeta_m-\zeta_k)(\zeta_m-\bar{\zeta}_k)}\right] \tag{B3}$$

where the overbar denotes the complex conjugate,

$$A_{ij}(\mathbf{n}) = adj\,[c_{ikjl}\,n_k\,n_l], \qquad D(\mathbf{n}) = \det\,[c_{ikjl}\,n_k\,n_l] \tag{B4}$$

p and **q** are two vectors related to the field points, and a_k are the coefficients of the sixth-order polynomial $D(\mathbf{n})$, i.e.

$$D(\mathbf{p}+\zeta\mathbf{q}) = \sum_{k=0}^{6} a_{k+1}\zeta^k = a_7 \prod_{m=1}^{3} (\zeta-\zeta_m)(\zeta-\bar{\zeta}_m) \tag{B5}$$

The three roots $\zeta_m (m = 1, 2, 3)$ are chosen with $\mathrm{Im}\,\zeta_m > 0$. Expressions for the traction Green's functions and their derivatives are much complicated, and they can be obtained by the efficient and accurate numerical method proposed in Tonon *et al.* [36].

APPENDIX C: SHAPE FUNCTIONS FOR UNCRACKED BOUNDARY

Shape functions for type I *element on the uncracked boundary*

$$\begin{aligned}
\phi_1 &= 0.25\xi\eta(\xi-1)(\eta-1)\\
\phi_2 &= 0.5\eta(1-\xi^2)(\eta-1)\\
\phi_3 &= 0.25\xi\eta(\xi+1)(\eta-1)\\
\phi_4 &= 0.5\xi(1-\eta^2)(\xi-1)\\
\phi_5 &= (1-\xi^2)(1-\eta^2)\\
\phi_6 &= 0.5\xi(1-\eta^2)(\xi+1)\\
\phi_7 &= 0.25\xi\eta(\xi-1)(\eta+1)\\
\phi_8 &= 0.5\eta(1-\xi^2)(\eta+1)\\
\phi_9 &= 0.25\xi\eta(\xi+1)(\eta+1)
\end{aligned} \tag{C1}$$

Shape functions for type II *element on the uncracked boundary*

$$\begin{aligned}
\phi_1 &= 0.45\xi\eta(\xi-1)(\eta-1)\\
\phi_2 &= 0.9\eta(1-\xi^2)(\eta-1)\\
\phi_3 &= 0.45\xi\eta(\xi+1)(\eta-1)\\
\phi_4 &= 0.75\xi(1-\eta)(2/3+\eta)(\xi-1)\\
\phi_5 &= 1.5(\xi^2-1)(\eta-1)(2/3+\eta)\\
\phi_6 &= 0.75\xi(1-\eta)(2/3+\eta)(\xi+1)\\
\phi_7 &= 0.3\xi\eta(\xi-1)(2/3+\eta)\\
\phi_8 &= 0.6\eta(1-\xi^2)(2/3+\eta)\\
\phi_9 &= 0.3\xi\eta(\xi+1)(2/3+\eta)
\end{aligned} \tag{C2}$$

Shape functions for type III *element on the uncracked boundary*

$$
\begin{aligned}
\phi_1 &= 0.81\xi\eta(\xi-1)(\eta-1)\\
\phi_2 &= 1.35\eta(1-\xi)(2/3+\xi)(\eta-1)\\
\phi_3 &= 0.54\xi\eta(2/3+\xi)(\eta-1)\\
\phi_4 &= 1.35\xi(1-\eta)(2/3+\eta)(\xi-1)\\
\phi_5 &= 2.25(1-\xi)(2/3+\xi)(1-\eta)(2/3+\eta)\\
\phi_6 &= 0.9\xi(1-\eta)(2/3+\eta)(2/3+\xi)\\
\phi_7 &= 0.54\xi\eta(\xi-1)(2/3+\eta)\\
\phi_8 &= 0.9\eta(2/3+\eta)(1-\xi)(2/3+\xi)\\
\phi_9 &= 0.36\xi\eta(2/3+\xi)(2/3+\eta)
\end{aligned}
\tag{C3}
$$

Shape functions for type IV element on the uncracked boundary

$$
\begin{aligned}
\phi_1 &= 0.54\xi\eta(\xi-2/3)(\eta-1)\\
\phi_2 &= -1.35\eta(1+\xi)(\xi-2/3)(\eta-1)\\
\phi_3 &= 0.81\xi\eta(\xi+1)(\eta-1)\\
\phi_4 &= 0.9\xi(1-\eta)(2/3+\eta)(\xi-2/3)\\
\phi_5 &= -2.25(1+\xi)(\xi-2/3)(1-\eta)(2/3+\eta)\\
\phi_6 &= 1.35\xi(1-\eta)(2/3+\eta)(\xi+1)\\
\phi_7 &= 0.36\xi\eta(\xi-2/3)(2/3+\eta)\\
\phi_8 &= -0.9\eta(2/3+\eta)(1+\xi)(\xi-2/3)\\
\phi_9 &= 0.54\xi\eta(\xi+1)(2/3+\eta)
\end{aligned}
\tag{C4}
$$

ACKNOWLEDGEMENTS

The work presented in this paper was supported by National Science Foundation under Grant CMS-9713559, Air Force Office of Scientific Research under Grant F33615-97-C-5089 and F49620-98-1-0104.

REFERENCES

1. Cruse TA. *Boundary Element Analysis in Computational Fracture Mechanics*. Kluwer Academic Publishers: Dordrecht, The Netherlands, 1988.
2. Aliabadi MH. Boundary element formulations in fracture mechanics. *Applied Mechanics Review* 1997; **50**:83–96.
3. Pan E. A general boundary element analysis of 2-D linear elastic fracture mechanics. *International Journal of Fracture* 1997; **88**:41–59.
4. Snyder MD, Cruse TA. Boundary-integral analysis of anisotropic cracked plates. *International Journal of Fracture* 1975; **11**:315–328.

5. Blandford GE, Ingraffea AR, Liggett JA. Two-dimensional stress intensity factor computations using the boundary element method. *International Journal for Numerical Methods in Engineering* 1981; **17**:387–404
6. Crouch SL, Starfield AM. *Boundary Element Methods in Solid Mechanics*. George Allen and Unwin Publishers: London, 1983.
7. Pan E. Dislocation in an infinite poroelastic medium. *Acta Mechanica* 1991; **87**:105–115.
8. Sirtori S, Maier G, Novati G, Miccoli S. A Galerkin symmetric boundary-element method in elasticity: Formulation and implementation. *International Journal for Numerical Methods in Engineering* 1992; **35**:255–282.
9. Portela A, Aliabadi MH, Rooke DP. Dual boundary element method: Efficient implementation for cracked problems. *International Journal for Numerical Methods in Engineering* 1992; **33**:1269–1287.
10. Mi Y, Aliabadi MH. Dual boundary element method for three-dimensional fracture mechanics analysis. *Engineering Analysis with Boundary Elements* 1992; **10**:161–171.
11. Pan E, Amadei B. Fracture mechanics analysis of cracked 2-D anisotropic media with a new formulation of the boundary element method. *International Journal of Fracture* 1996; **77**:161–174.
12. Qin TY, Chen WJ, Tang RJ. Three-dimensional crack problem analysis using boundary element method with finite-part integrals. *International Journal of Fracture* 1997; **84**:191–202.
13. Sohn GH, Hong CS. Application of singular integral equations to embedded planar crack problems in finite body. In Brebbia AC, Maier G (eds). *Boundary Element*, Vol. 2, Springer: Berlin, 1985; 8-57–8-67.
14. Wong GK, Barnett DM. A dislocation method for solving 3-D crack and inclusion problems in linear elastic solids. In Bilby AB (ed.). *Fundamentals of Deformation and Fracture*, *Eshelly Memorial Symposium*, Cambridge University Press: Cambridge, 1985; 417–437.
15. Gray LJ, Martha LF, Ingraffea AR. Hypersingular integrals in boundary element fracture analysis. *International Journal for Numerical Methods in Engineering* 1990; **29**:1135–1158.
16. Martha LF, Gray LJ, Ingraffea AR. Three-dimensional fracture simulation with a single-domain direct boundary element formulation. *International Journal for Numerical Methods in Engineering* 1992; **35**:1907–1921.
17. Qin TY, Tang RJ. Finite-part integral and boundary element method to solve embedded planar crack problems. *International Journal of Fracture* 1993; **60**:373–381.
18. Zhao M, Liu Y, Cheng C. Boundary-integral equations and the boundary-element method for three-dimensional fracture mechanics. *Engineering Analysis with Boundary Elements* 1994; **13**:333–338.
19. Xu Y, Moran B, Belytschko T. Self-similar crack expansion method for three-dimensional crack analysis. ASME, *Journal of Applied Mechanics* 1997; **64**:729–737.
20. Xu Y, Moran B, Belytschko T. Self-similar crack expansion method for three-dimensional cracks under mixed-mode loading conditions. ASME, *Journal of Applied Mechanics* 1998; **65**:557–565.
21. Sladek V, Sladek J. Three-dimensional crack analysis for an anisotropic body. *Applied Mathematical Modelling* 1982; **6**:374–381.
22. Kassir MK, Sih GC. Three-dimensional stresses around elliptical cracks in transversely isotropic solids. *Engineering Fracture Mechanics* 1968; **1**:327–345.
23. Hoenig A. The behavior of a flat elliptical crack in an anisotropic elastic body. *International Journal of Solids and Structures* 1978; **14**:925–934.
24. Zhang ZG, Mai YW. A simple solution for the stress intensity factor of a flat elliptical crack in a transversely isotropic solid. *Engineering Fracture Mechanics* 1989; **34**:645–648.
25. Ishikawa H. Application of the boundary element method to anisotropic crack problems. In Aliabadi MH, Brebbia CA (eds). *Advances in Boundary Element Methods for Fracture Mechanics*, Computational Mechanics Publications: Southampton, UK, 1993; 269–291.
26. Kutt HR. Quadrature formulae for finite-part integrals. *Special Report WISK* 178, National Research Institute for Mathematical Sciences, Pretoria, 1975.
27. Kutt HR. On the numerical evaluation of finite-part integrals involving an algebraic singularity. *Special Report WISK* 179, National Research Institute for Mathematical Sciences, Pretoria, 1975.
28. Pan E, Amadei B. A 3-D boundary element formulation of anisotropic elasticity with gravity. *Applied Mathematical Modelling* 1996; **20**:114–120.
29. Lin W, Keer LM. Three-dimensional analysis of cracks in layered transversely isotropic media. *Proceedings of Royal Society* (*London*) 1989; **A424**:307–322.
30. Brebbia CA, Dominguez J. *Boundary Element Methods*, *An Introductory Course*. McGraw-Hill: New York, 1989.
31. Ting TCT. *Anisotropic Elasticity*: *Theory and Applications*. Oxford University Press: Oxford, 1996.
32. Sih GC, Paris PC, Irwin GR. On cracks in rectilinearly anisotropic bodies. *International Journal of Fracture* 1965; **3**:189–203.
33. Hoenig A. Near-tip behavior of a crack in a plane anisotropic elastic body. *Engineering Fracture Mechanics*. 1982; **16**:393–403.
34. Suo Z. Singularities, interfaces and cracks in dissimilar anisotropic media. *Proceedings of the Royal Society* (*London*), 1990; **A427**:331–358.
35. Pan YC, Chou TW. Point force solution for an infinite transversely isotropic solid. ASME *Journal of Applied Mechanics* 1976; **43**:608–612.

36. Tonon F, Pan E, Amadei B. Green's functions and BEM formulation for 3D anisotropic media. *Computers and Structures* 1999; submitted.
37. Tada H, Paris PC, Irwin GR. *The Stress Analysis of Cracks Handbook* (2nd edn). Paris Productions Incorporated: Missouri, 1985.
38. Weaver J. Three-dimensional crack analysis. *International Journal of Solids and Structures*. 1997; **13**: 321–330.
39. Murakami Y. *Stress Intensity Factors Handbook*. Pergamon Press: Oxford, 1987.
40. Wen PH, Aliabadi MH. Mixed-mode weight functions in three-dimensional fracture mechanics: static. *Engineering Fracture Mechanics* 1998; **59**:563–575.

